Bio-Design and Manufacturing (2025) 8:948–961
https://doi.org/10.1631/bdm.2500183

RESEARCH ARTICLE

Development of novel microtubular ionic actuators for endovascular navigation

Qingsong He[1,2,3] · Siyuan Liu[1] · Xiaofang Liu[1] · Weixiang Gao[1,3] · Zhihao Lv[1,4] · Xin Shen[1] · Jinjun Duan[1] · Yunfei Han[5] · Jianfeng Zhao[1] · Ying Hu[6] · Wenqi Liu[7] · Fengjiang Zhan[3] · Longfei Chang[6] · Tao Wang[6] · Yuze Ye[1] · Qiyun Zhong[1,3] · Xinyu Lu[1,3] · Weiming Xu[1] · Yefu Wang[8] · Yang Gu[9] · Chenchu Zhang[6] · Dong Wu[10] · Yong Li[8]

Received: 12 April 2025 / Accepted: 22 July 2025 / Published online: 27 October 2025

Abstract

Minimally invasive interventional surgery techniques using guidewire-based catheters are widely adopted to treat vascular diseases. However, commonly used interventional catheters lack active guidance. The use of guidewires is associated with risks, including increased exposure to X-rays and potential vascular damage during withdrawal from complex vessels. Herein, we developed sub-millimeter microtubular ionic actuators (0.6–0.8 mm outer diameter) integrated into steerable interventional catheters. These actuators can generate large deformations (>10 mm) under 7 V direct current due to enhanced ion migration, enabling precise navigation without the need for guidewires. The designed catheters achieved active bending and accurate positioning in complex arterial vascular branches within a human model. They were also able to navigate within different arterial locations (e.g., the innominate, subclavian, and carotid arteries) in pigs without the use of guidewires, and even access the ventricle and deliver contrast medium, indicating their great potential for future endovascular therapy.

✉ Qingsong He
heqingsong@nuaa.edu.cn

✉ Ying Hu
huying@hfut.edu.cn

✉ Yong Li
liyongmydream@126.com

1 Jiangsu Provincial Key Laboratory of Bionic Materials and Equipment, College of Mechanical and Electrical Engineering, Nanjing University of Aeronautics and Astronautics, Nanjing 210016, China

2 State Key Laboratory of Mechanics and Control for Aerospace Structures, Nanjing University of Aeronautics and Astronautics, Nanjing 210016, China

3 Key Laboratory of Advanced Technology for Small and Medium-sized UAV, Ministry of Industry and Information Technology, Unmanned Aerial Vehicles Research Institute, Nanjing University of Aeronautics and Astronautics, Nanjing 210016, China

4 Center for X-Mechanics, Department of Engineering Mechanics, Zhejiang University, Hangzhou 310027, China

5 Department of Neurology, Affiliated Hospital of Nanjing University of Chinese Medicine, Nanjing 210023, China

6 Anhui Province Key Lab of Aerospace Structural Parts Forming Technology and Equipment, School of Materials Science and Engineering, Hefei University of Technology, Hefei 230009, China

7 Innovation Center of Genesis MedTech Group, Wuxi 214000, China

8 Department of Cardiology, The First Affiliated Hospital of Nanjing Medical University, Nanjing 210029, China

9 Department of Cardiology, The Affiliated Huaian No. 1 People's Hospital of Nanjing Medical University, Huai'an 223300, China

10 CAS Key Laboratory of Mechanical Behavior and Design of Materials, Department of Precision Machinery and Precision Instrumentation, University of Science and Technology of China, Hefei 230027, China

Graphical abstract

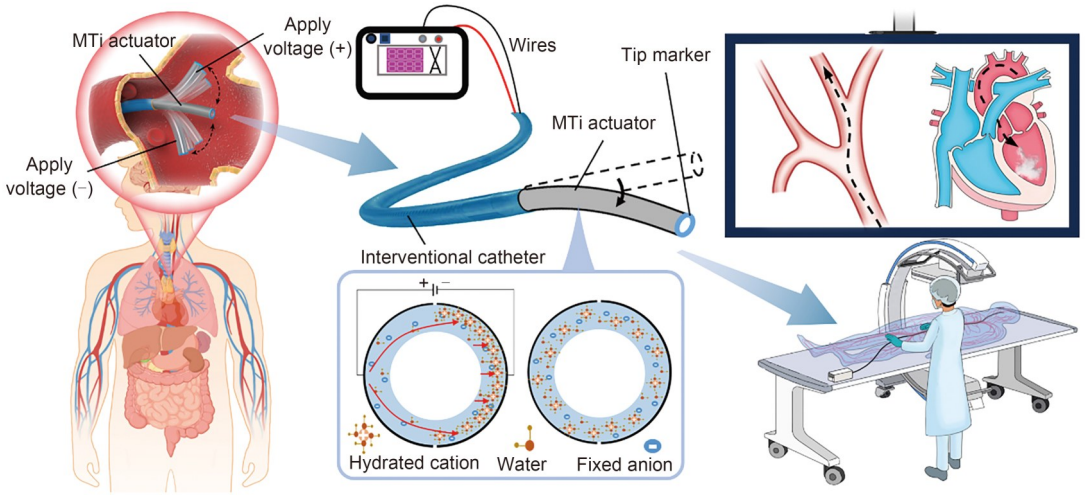

Keywords Microtubular ionic (MTi) actuators · Steerable interventional catheters · Endovascular navigation · Endovascular therapy · Contrast medium delivery

1 Introduction

Vascular diseases pose a serious threat to human health (Fig. 1a). Endovascular therapy is the most direct and effective clinical method for treating such diseases, as it offers high accuracy, short recovery time, high safety, fewer postoperative complications, and less trauma compared to traditional open surgery [1]. In general, the diameter of the aortic vessels in adults is less than 30 mm, and the diameter of the blood vessels decreases with age. Moreover, the blood vessels of patients with atherosclerosis are typically narrowed and tortuous, necessitating the use of guidewires to guide catheters to these relevant vessel sites [2]. Moreover, in small and curved arteries, interventional catheters must be shaped externally through multiple passes of the guidewires, and then pushed, pulled, and twisted by the physician to reach the lesion, which increases exposure time to X-rays. During withdrawal from the lesion site, the guidewires may rub against the walls of complex blood vessels, causing severe pain or even serious consequences such as rupture and perforation of the blood vessels.

Recently, steerable catheters based on smart actuators with tip-bending capabilities have been developed, which can potentially enable active guidance within the vessel without the use of guidewires. The primary actuation methods to realize tip bending include magnetic [3–6], Bowden cable [7–9], hydraulic [10–15], thermal [16–21], and electric [21–25] actuation. Among these, ionic electrochemical actuators, composed of materials such as ionic polymer–metal composites, conductive polymers, and carbon nanomaterials, can use electricity as a stimulation source. These actuators can provide low-voltage actuation, are suitable for liquid environments, and offer controllable deformation [26–36], making them excellent candidates for imparting interventional catheters with active guiding capabilities. Previously, researchers applied sheet- and column-shaped ionic actuators to the end of catheters and verified their ability to guide the catheters in vitro [37–41]. Although the columnar ionic actuators are geometrically similar to catheters, their solid structure prevents them from delivering contrast media or other medical devices into blood vessels for arteriography or therapeutic effects, further limiting their applications as manipulable catheters in interventional therapy.

These challenges can be overcome using hollow tubular ionic actuators, as previously reported [42–45]. However, their actuation performance was relatively low and could not meet the actual clinical surgery requirements for endovascular therapy. More importantly, the sizes of these tubular ionic actuators generally do not match those of the interventional catheters used in surgeries. To accommodate narrow and elongated vascular sites, the diameter of interventional catheters (such as Excelsior, Marathon, Cordis, TERUMO, and PIONEER) commonly used in vascular interventions should be less than 2 mm (Table S1 in the supplementary information) [46–49]. To adapt to the small size of these catheters and achieve the desired position within narrow blood vessels, the tubular ion actuators should be less than 1 mm in diameter, which has not yet been achieved. Furthermore, in vitro and in vivo clinical trials have not been conducted to validate these actuators for use with interventional catheters for active navigation under electrical voltage. Therefore, the use of microtubular ionic actuators with

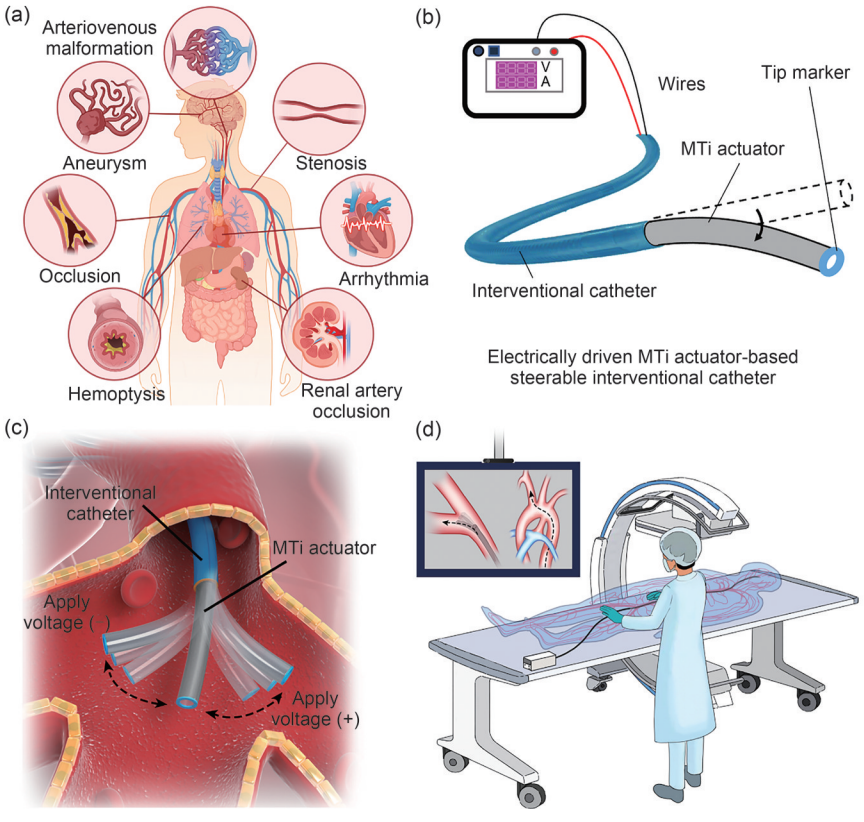

Fig. 1 A schematic diagram of the microtubular ionic (MTi) actuator-based steerable interventional catheters. (a) Schematic diagram showing the use of interventional therapy in treating vascular diseases. (b) The structure of the electrically driven MTi actuator-based steerable interventional catheters. A tip marker at the end of the MTi actuators enables precise observation of their deformable position within blood vessels. (c) The bending deformation of the MTi actuators after applying positive or negative voltage for active navigation of the catheters in complex vascular systems. (d) The steerable interventional catheters can actively navigate and rapidly pass through complex blood vessels in the human body to reach designated locations without the need for guidewires

high-performance actuation capabilities, combined with steerable interventional catheters, should be explored in interventional vascular surgery.

Here, we designed microtubular ionic (MTi) actuators that provide large bending deformations under low electrical voltages, and integrated them with interventional catheters to construct electrically driven steerable catheters that can navigate actively without the use of guidewires in vascular therapy. These MTi actuators, of different sizes (inner diameter/outer diameter: 0.3 mm/0.6 mm and 0.6 mm/0.8 mm, abbreviated as 0.6- and 0.8-MTi actuators), were prepared using a chemical plating method to adapt to blood vessels of varying sizes. The steerable interventional catheters were developed by installing the MTi actuators at their tip to achieve active bidirectional bending under voltage (Fig. 1b). Furthermore, a tip marker visible under X-ray was installed at the tip of the controllable interventional catheters to visualize the deformable position of the catheter's tip in the blood vessel during the interventional procedures. The MTi actuators showed controllable deformation (13.06 mm) and a large bending angle (1.31 (°)/mm) under low voltage (4–7 V direct current (DC)), indicating their excellent performance. Therefore, these electrically driven steerable interventional catheters offer significant flexibility and controllability in highly restricted environments, such as actively navigating in narrow and tortuous vascular systems under positive or negative voltage (Fig. 1c), warranting further investigations using human clinical trials (Fig. 1d). Using pigs as a test model, the catheters could be successfully positioned in the innominate, right subclavian, common carotid, left common carotid, and right common carotid arteries, as well as the left ventricle through active steering deformation. Furthermore, the hollow structure of these MTi actuators enabled the delivery of contrast medium. These results demonstrate the potential of steerable interventional catheters for future interventional therapies in vascular diseases.

2 Materials and methods

2.1 Materials

TT020 and TT030 (two types of Nafion^{TM} tubing with different inner and outer diameters; the inner and outer diameters of

TT020 are 0.3 and 0.6 mm, respectively, while for TT030 they are 0.6 and 0.8 mm), which were used for the ionic polymer tube, were purchased from Perma Pure (USA). The chemical plating solution comprised ammonia solution ($NH_3{\cdot}H_2O$) and platinum ammonia complex ($[Pt(NH_3)_4]Cl_2$). Sodium hydroxide (NaOH), hydroxylamine hydrochloride ($NH_2OH{\cdot}HCl$), hydrazine hydrate ($N_2H_4{\cdot}1.5H_2O$), and sodium borohydride ($NaBH_4$) were used as reducing agents for preparing the platinum ammonia complexes. Lithium chloride (LiCl) and lithium hydroxide (LiOH) were used to prepare ion exchange solutions. Dilute hydrochloric acid (HCl) was used to remove other impurities. The conductivity of the tube was increased using LiCl. All chemical reagents were purchased from Sigma-Aldrich (USA).

2.2 Fabrication of the MTi actuators

Abrasives and metallographic polishing cloth were used to roughen the outer surface of the Nafion tube, thereby expanding the interfacial area. Platinum electrodes were deposited on the outer surface of Nafion tubes by chemical plating [35, 36, 39]. Then, the Nafion tube was boiled in HCl and then in deionized water at 80 °C to eliminate impurities. The treated Nafion tube was soaked in a mixed solution of $[Pt(NH_3)_4]Cl_2$ and $NH_3{\cdot}H_2O$ (5%) for 12 h. $NaBH_4$ (1.5%) and NaOH (0.5%) were used as reducing agents during chemical plating at 42–62 °C for 6.5 h. After the reaction, the prepared MTi actuators were immersed in HCl (0.5%) for 8 h and then in a mixture of $[Pt(NH_3)_4]Cl_2$ and $NH_3{\cdot}H_2O$ (5%), with $NH_2OH{\cdot}HCl$ (1.5%) and $N_2H_4{\cdot}1.5H_2O$ (20%) as the reducing agents at 42–62 °C for 5 h. After that, the MTi actuators were soaked in HCl (0.5%) for 8 h, and then stored in a mixture of LiCl and LiOH solution.

2.3 Characterization of the MTi actuators

A multimeter was used to conduct resistance tests on the surface electrodes of the MTi actuators. On each MTi actuator sample, the resistance was measured at five positions on both the front and back electrode surfaces, with electrodes 10 mm apart. The average electrode resistance of each sample was calculated. The thickness of the electrode and its bonding with the basal canal were observed using a field-emission scanning electron microscope (SEM; Helios 5 CX, USA).

A force sensor (Q84X5X12-05, Zhonghang Electronic Measuring Instruments Co., Ltd., China) was used for testing the blocking force in air. The sample was placed vertically and fixed at the top. The outer surface of the free end of the sample was gently contacted with the working surface of the force sensor at a distance of 2 mm. By applying different voltages to the fixed end of the sample, data on the blocking force can be obtained. Tip displacement testing was performed using a laser displacement sensor (LK-80, KEYENCE, Japan). The sample length was 41 mm. The test tip displacement data were obtained at a distance of 10 mm from the free end. During the displacement testing process, the sample was connected in a series circuit with a 10 Ω resistor. By collecting voltage data from two resistance segments, the variation curve of the sample current can be obtained.

2.4 Electrochemical testing

Electrochemical testing was conducted using electrochemical analyzers (CHI604, Shanghai Chenhua Instruments Co., China). The auxiliary and reference electrodes of the electrochemical analyzer were connected to one electrode of the MTi actuator, while the working electrode was connected to the other electrode. The current (C)–voltage (V) curve of the MTi actuators was obtained using the voltammetry cycle method, with a lower limit potential of −0.5 V and an upper limit potential of 0.5 V. The scanning speeds were 100, 200, 400, 600, and 800 mV/s. The electrochemical impedance of the MTi actuators was measured using alternating current (AC) impedance spectroscopy with a scanning frequency range of 10^{-2}–10^5 Hz.

2.5 Finite element simulation

To analyze the electrical actuation performance, a three-dimensional (3D) model of the MTi actuator was established using COMSOL Multiphysics. The electrode surface was defined with Dirichlet boundary conditions. The upper 6-mm-thick surface of the MTi actuator model was set as a fixed constraint, which was consistent with the actual constraint conditions. To ensure the accuracy of the finite element simulation, an unstructured tetrahedral mesh division was adopted to accommodate complex regions and boundary calculations. The structural parameters of the model were consistent with those of the experiment.

2.6 Fabrication of steerable interventional catheters

As shown in Fig. S1 (supplementary information), two wires were welded onto both electrodes of the MTi actuator and were insulated except at the welding points. The other ends of the wires were connected to the power supply. The outer wall of the MTi actuator was tightly attached to the inner wall of the intervention catheters, and the welding points were located between these walls. Silicone rubber was used to seal the space between the MTi actuator and the intervention catheter to prevent electrical leakage and vascular damage.

2.7 In vivo animal experiment in pigs

Animal procedures were conducted according to the ethical regulations reviewed and approved by the Institutional Animal

Care and Use Committee (approval No. IACUC-2306014) at the First Affiliated Hospital with Nanjing Medical University. A female Bama miniature pig (35 kg) was selected as the experimental model. Before the experiment, the steerable interventional catheters were exposed to physiological saline during angiography procedures. The model was anesthetized using a combination of midazolam and atropine. After anesthesia, the model was fixed on the surgical platform, and tracheal intubation was performed orally. Intravenous injection was used to maintain anesthesia during surgery (propofol at 1 mg/(kg·h)). Oxygen was supplied continuously at a flow rate of 2 mL/min. The test pig was placed face up on the operating table.

3 Results and discussion

3.1 Fabrication and characterization of the MTi actuators

MTi actuators can bend reversibly in air, deionized water, and physiological saline when subjected to an external electrical potential. The detailed deformation mechanism is illustrated in Fig. 2a. When a voltage is applied to the electrodes of the MTi actuator, the hydrated cations within the Nafion tube undergo directional migration toward the cathode due to the electric field. This results in an asymmetric deformation of the electrodes on both sides of the MTi

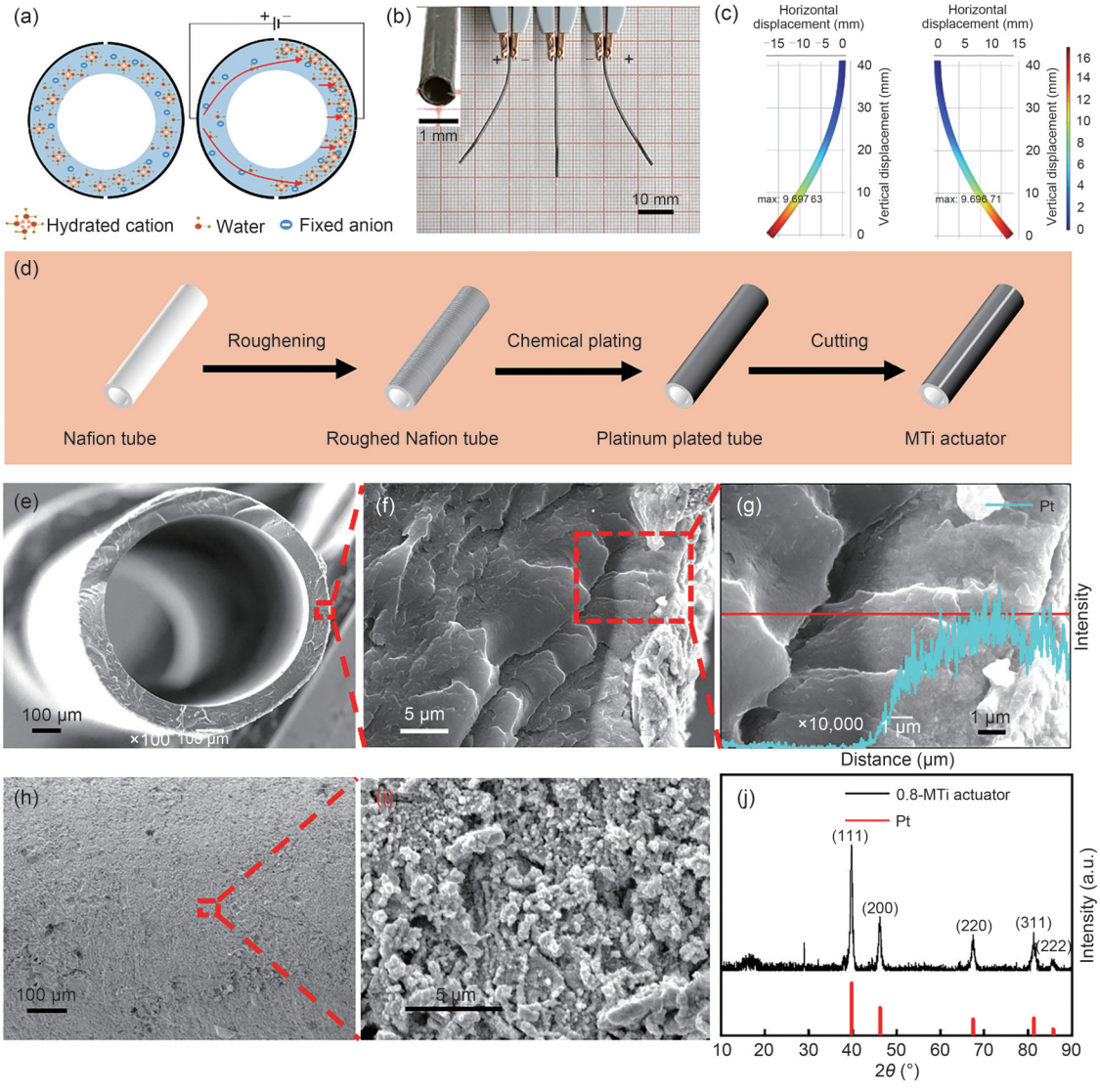

Fig. 2 Fabrication and characterization of the MTi actuators. (a) A schematic diagram of the actuation mechanism of the MTi actuators based on the electrochemical-induced ion migration. (b) Optical images of the bending deformation of the 0.8-MTi actuators under 7 V electrical voltage in air. The inset shows the cross-section of the MTi actuator. (c) Finite element simulation of the electrical-driven bending deformation of the 0.8-MTi actuators. (d) Fabrication process of the MTi actuators. (e, f) Cross-sectional SEM images of the 0.8-MTi actuators from low to high magnification. (g) EDS image of the electrode. (h, i) Surface images of the electrode of the 0.8-MTi actuators from low to high magnification. (j) XRD pattern of the electrode of the 0.8-MTi actuators

actuators. Due to the presence of more hydrated cations in the cathode region, the expansion deformation is more significant in this part, which in turn causes the entire MTi actuator to bend toward the anode. The detailed actuation bending performance of the MTi actuators with different tube diameters under electrical voltage in air is shown in Fig. 2b, Fig. S2, and Movie S1 (supplementary information). It can be seen that the actuators produced reversible bending deformation under electrical voltage, and the direction of the voltage controlled the direction of deformation. The deformation process was also analyzed using finite element simulation, and the results were consistent with those obtained experimentally (Fig. 2c).

As shown in Fig. 2d, the MTi actuator consists of an outer noble metal electrode (platinum, Pt) and an inner ionic Nafion tube polymer. To ensure the safety of the catheters during interventional surgery, the electrode should be smooth and tightly bonded to the polymer membrane to prevent both electrode detachment and any resulting damage to blood vessels and the human body. The cross-section SEM images of the MTi actuators show their varying diameters (Figs. 2e and 2f; Figs. S3a and S3b in the supplementary information). The electrodes of the MTi actuators were uniform and dense, without any gaps between the deposited electrode and the surface of the Nafion tube. This prevents the electrode from cracking or peeling off the surface of the Nafion tube when the actuators undergo significant deformation. Energy-dispersive spectrometry (EDS) of the MTi actuators further shows that the Pt ions adsorbed inside the Nafion tube are reduced to Pt nanoparticles on the surface of the tube, forming the Pt electrode (Fig. 2g). Furthermore, a small amount of Pt element permeates into the interior of the Nafion tube at the interface, which can provide larger interfacial area and better contact performance between the electrode and the Nafion tube (Fig. 2g; Fig. S3c in the supplementary information). Observation of the microstructure of the surface electrodes of the MTi actuators revealed the uniform distribution of nanoparticles on the surface of the Pt electrode (Figs. 2h and 2i; Figs. S3d and S3e in the supplementary information). Overall, the electrode is flat and continuous, without burrs or protrusions, which ensures that the MTi actuators will not puncture or scratch blood vessels during steering and insertion. As shown in Fig. 2j and Fig. S3f (supplementary information), the X-ray diffraction (XRD) patterns of the MTi actuators' electrode indicate characteristic diffraction peaks at 39.8°, 46.2°, 67.5°, 81.3°, and 85.7°, corresponding to the (111), (200), (220), (311), and (222) crystal planes of Pt, further validating the presence of the Pt electrode.

The surface resistance of the MTi actuator was measured because the actuation performance of ionic actuators depends on their electrode properties. The 0.6-MTi electrode of the actuators, with an outer diameter of 0.6 mm, had an average surface resistance value of 3.2 Ω/cm, while this value was 4.8 Ω/cm for the 0.8-MTi actuators, with an outer diameter of 0.8 mm (Table S2 in the supplementary information). These results demonstrate the excellent electrical conductivity of the MTi actuators' electrodes, which facilitates the migration of ions within the Nafion polymer under an applied electrical voltage.

3.2 Electro-chemical-mechanical properties

As the actuation performance of the MTi actuator depends on ion migration, actuators with high electrochemical capacitance characteristics exhibit a substantial deformation effect. Cyclic voltammetry curves were measured at different scan rates for the MTi actuators to investigate their capacitance characteristics (Figs. 3a and 3b). A typical double-layer capacitance was observed, with no prominent oxidation peaks. The specific capacitance of the MTi actuators gradually decreases as the scan rate increases (Fig. S4 in the supplementary information). At a scan rate of 100 mV/s, the specific capacitances of the 0.6- and 0.8-MTi actuators were 13.31 and 9.76 mF/g, respectively. When the scan rate was increased to 800 mV/s, the specific capacitances of the 0.6- and 0.8-MTi actuators decreased to 6.12 and 4.43 mF/g, respectively. Notably, the specific capacitance of the 0.6-MTi actuator is larger than that of the 0.8-MTi actuator, mainly due to the lower resistance and higher current (Tables S2 and S3 in the supplementary information) of the 0.6-MTi actuator's electrode compared with that of the 0.8-MTi actuator.

Electrochemical impedance spectroscopy was performed to evaluate the ion kinetic diffusion and storage properties of the MTi actuators (Figs. 3c and 3d). In the Nyquist plot, the depressed semicircle indicates a high frequency, while the straight line represents a low frequency. These features are mainly attributed to charge transfer and ionic diffusion, respectively. As shown in the Bode plot, the impedance of both actuators increases as the frequency decreases. In the high-frequency region, the impedance of the 0.6-MTi actuator is lower than that of the 0.8-MTi actuator, while this trend is reversed in the low-frequency region. This suggests that reducing the diameter of the actuators can decrease resistance and enhance capacitance characteristics. In the high-frequency range, the phase angles of the two actuators are almost the same. In the low-frequency range, the phase angle of the 0.6-MTi actuators is higher than that of the 0.8-MTi actuators. As the frequency decreases, the phase angle in the high-frequency region of the Bode plot tends to decrease, indicating the presence of typical capacitance resistance (RC) coupling behavior in the system. In contrast, the phase angle in the low-frequency region shows an increasing trend, indicating the presence of diffusion impedance (such as Warburg diffusion impedance). In the equivalent circuit (inset of Fig. 3c; Table S3 in the supplementary

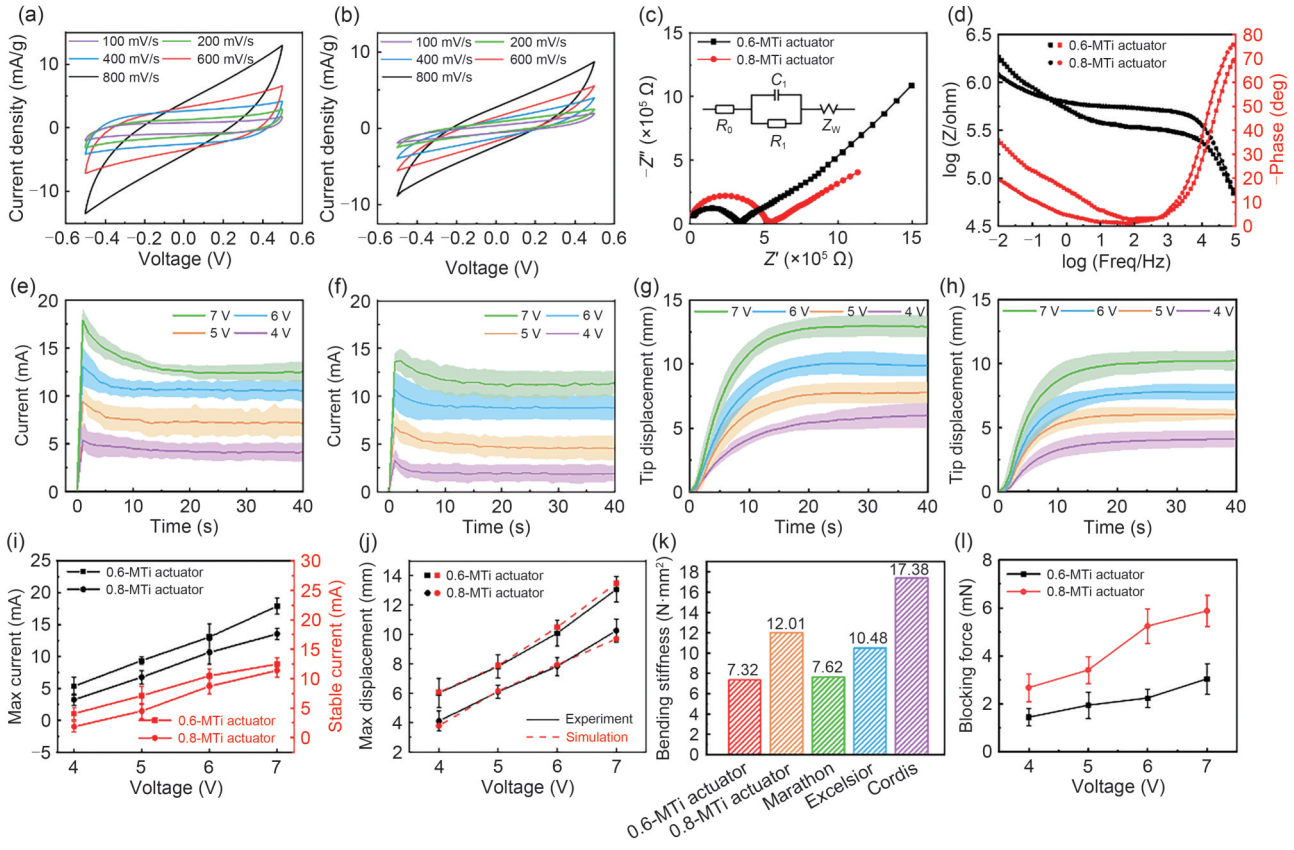

Fig. 3 Electrochemical actuation of the MTi actuators. Cyclic voltammetry characteristic of the 0.6-MTi (a) and 0.8-MTi (b) actuators at different scan rates in air. (c) Nyquist plots of the MTi actuators. The inset shows the equivalent circuit model. (d) Bode plots of the MTi actuators. Current change of the 0.6-MTi (e) and 0.8-MTi (f) actuators in air. Maximum tip displacement of the 0.6-MTi (g) and 0.8-MTi (h) actuators in air. Maximum and stable current (i) and maximum tip displacement (j) of the MTi actuators with different voltages in air. (k) Comparison of bending stiffness between MTi actuators of different diameters and traditional interventional catheters. (l) The generated blocking force of the MTi actuators under different electrical voltages in air. Data in (i, j, l) are expressed as mean±standard deviation (n=3)

information), R_0 and R_1 represent the ohmic resistance of the actuators and the charge transfer resistance, respectively. The Warburg diffusion element Z_W indicates the ion diffusion ability in the actuators. The elements C_1/R_1 in parallel represent the contact impedance, reflecting the electron conduction from the metal electrode to the actuator's electrode. These results demonstrate that the MTi actuators possess good electrical contact, ion diffusion ability, and energy storage capacity, which is beneficial for electrochemical actuation.

Furthermore, the electrical current of the ionic actuators under an electrical voltage is related to internal ion migration, which determines the actuator's deformation. Therefore, the currents of the MTi actuators operated in air, deionized water, and physiological saline under different voltages were tested (Figs. 3e, 3f, and 3i; Figs. S5a–S5f in the supplementary information). Initially, the hydrated cations in MTi actuators migrated rapidly in response to the electrical voltage, resulting in a sudden increase in current. As the cations gradually distribute and rearrange within the material, the current decreases and eventually stabilizes. At a voltage of 7 V DC, the average stable current values of the 0.6- and 0.8-MTi actuators in air are 12.50 and 11.41 mA, respectively. In deionized water, these values are 16.58 and 14.86 mA, respectively, which are similar to those seen in physiological saline. As shown in Tables S4–S6 (supplementary information), the maximum difference in current at 7 V DC is only 3.2%. At the same voltage, the narrower MTi actuators exhibited higher peak currents (1.22–1.64 times in air, 1.12–1.43 times in deionized water, and 1.13–1.46 times in physiological saline), indicating that shorter electrode spacing can generate greater instantaneous hydration cation migration.

Because the bending deformation of the MTi actuators installed at the catheter's tip enables its navigation within a specific vascular branch, actuators with large deformation displacement (bending angle) can adapt to more complex vascular branches. Figures 3g and 3h show the tip deformation displacement changes of the MTi actuators under different electrical voltages in air. Under voltage stimulation, the deformation displacement of the actuators first increases and then remains stable, indicating that the MTi actuators have fast deformation and good maintenance ability. Within a continuous stimulation of 40 s, the maximum bending

displacement of the 0.6- and 0.8-MTi actuators can reach 13.06 and 10.26 mm in air, respectively (Table S7 in the supplementary information). The bending displacement increases with the increase in the driving voltage (Fig. 3j), as shown by measuring the bending angle per unit length (Figs. S6 and S7 in the supplementary information). According to the test results (Tables S7–S9 in the supplementary information), the bending angle per unit length of the 0.6- and the 0.8-MTi actuators is 1.31 and 1.12 (°)/mm in air, 1.08 and 0.93 (°)/mm in deionized water, and 1.06 and 0.92 (°)/mm in physiological saline, respectively, under 7 V DC voltage. Furthermore, the actuators require slightly more time to reach a stable bending deformation displacement relative to their current change, as the hydrated cations in Nafion take some time to expand after being induced by the electrical field. Due to the larger ion migration and lower structural stiffness of 0.6-MTi actuators compared to the 0.8-MTi actuators, the former exhibit a larger tip displacement and bending angle per unit length than the latter under the same conditions. Moreover, using finite element simulation, we divided the grid of the MTi actuators with different diameters to verify their deformation displacement under voltage (Fig. S8 in the supplementary information). The specific simulation process is described in the experimental section. As shown in Fig. 3j and Figs. S9 and S10 (supplementary information), the maximum displacement distribution of the MTi actuators was compared across 4, 5, 6, and 7 V. The simulation results for maximum displacement at these voltages aligned with the experimental data. Each simulated value is within the error bands of the corresponding experimental measurements. The tip displacement of the MTi actuators under DC voltage in deionized water and physiological saline was also tested (Figs. S5g – S5l in the supplementary information). The MTi actuators are affected by frictional resistance when operated in deionized water, resulting in 18%–27% less deformation than in air. Under 4–7 V DC, the tip displacement of the MTi actuators in physiological saline differs by only 0.2%–3.6% from that in deionized water. Under continuous voltage stimulation, the MTi actuators can maintain a stable deformation state after reaching maximum deformation in a liquid environment, which aids in the active navigation of interventional catheters in vascular branches.

We also compared the bending stiffness of the MTi actuators with that of three commonly used interventional catheters, including Marathon, Excelsior, and Cordis catheters, as shown in Fig. 3k (detailed experimental testing methods are provided in the supplementary information). The bending stiffness of the 0.6-MTi actuators differs from that of the Marathon catheters by only 3.94%. The bending stiffness value of the 0.8-MTi actuators was between that of the Excelsior catheters and the Cordis catheters. This indicates that the bending stiffness values of the prepared MTi actuators are similar to those of the commonly used interventional catheters that are safe to use in blood vessels. Based on this information, the performance of these interventional catheters for active navigation in complex blood vessels was explored in vivo.

The blocking force is a crucial parameter for actuators that produce mechanical output. Figure 3l shows the blocking force of the MTi actuators under DC voltage in air. The output force of the MTi actuators with the same diameter increases with an increase in the driving voltage. At 7 V DC, the 0.8-MTi actuators can generate an output force of 5.9 mN, which facilitates stable steering and propulsion performance of the MTi actuator-based steerable catheters in vascular branches. However, this force is smaller in the 0.6-MTi actuators than that in the 0.8-MTi actuators, mainly due to the dual effects of internal ion migration and the stiffness of the actuators themselves on the output force of the actuators. Although the 0.6-MTi actuators have higher ion migration ability, the structural stiffness of the 0.8-MTi actuators is greater compared to the 0.6-MTi actuators. The structural stiffness of the actuators determines the overall mechanical performance, explaining the greater output force of the 0.8-MTi actuators. To further verify this phenomenon, a numerical simulation of the stress distribution in the MTi actuators was conducted. The results show that under 7 V, the stress of the 0.8-MTi actuators is significantly higher than that of the 0.6-MTi actuators (Fig. S11 in the supplementary information), further illustrating the importance of structural stiffness on output force.

We also summarized the essential characteristics of the MTi actuators (Table S2 in the supplementary information) and compared them with the other reported tubular ionic actuators (Table 1). The MTi actuators exhibit a significant improvement in micro-sized tube diameter, tip displacement, and blocking force compared to other tube-shaped ionic actuators [42, 45, 50].

3.3 In vitro experiment of the MTi actuator-based steerable interventional catheters in a human vascular model

The prepared MTi actuators were further assembled with interventional catheters to construct steerable interventional catheters, which can realize active bending under electrical voltage (Fig. 4a; Movie S2 in the supplementary information). The active navigation capacity of these catheters in blood vessels was evaluated using an in vitro experiment. The designed catheters were used to navigate from the aortic arch to the innominate, left subclavian, and left common carotid arteries under a specific electrical voltage. To better simulate the diameters of the aforementioned blood vessels, the Cordis catheter (6F, 1F≈0.333 mm) was selected as the main body of the steerable interventional catheters, and 0.8-mm

Table 1 Comparison of the characteristic parameters of the MTi actuators with other tube-shaped ionic actuators

Parameter	Tube-shaped ionic actuator [42]	Tube-shaped ionic actuator [45]	Tube-shaped ionic actuator [50]	This work	
Inner/Outer tube diameter (mm/mm)	1.3/1.6	2.4/3.0	2.18/2.74	0.3/0.6	0.6/0.8
Surface resistance (Ω/cm)	5.22	31	/	3.2	4.8
Input voltage (V)	6 DC	1 AC	3 DC	7 DC	7 DC
Maximum current (mA)	/	/	/	17.91	13.58
Maximum blocking force (mN)	2.5	5.42	1.75	3.0	5.9
Maximum tip displacement (mm)	3	0.15	3.5	13.06	10.26
Length (mm)	40	25	20	41	41

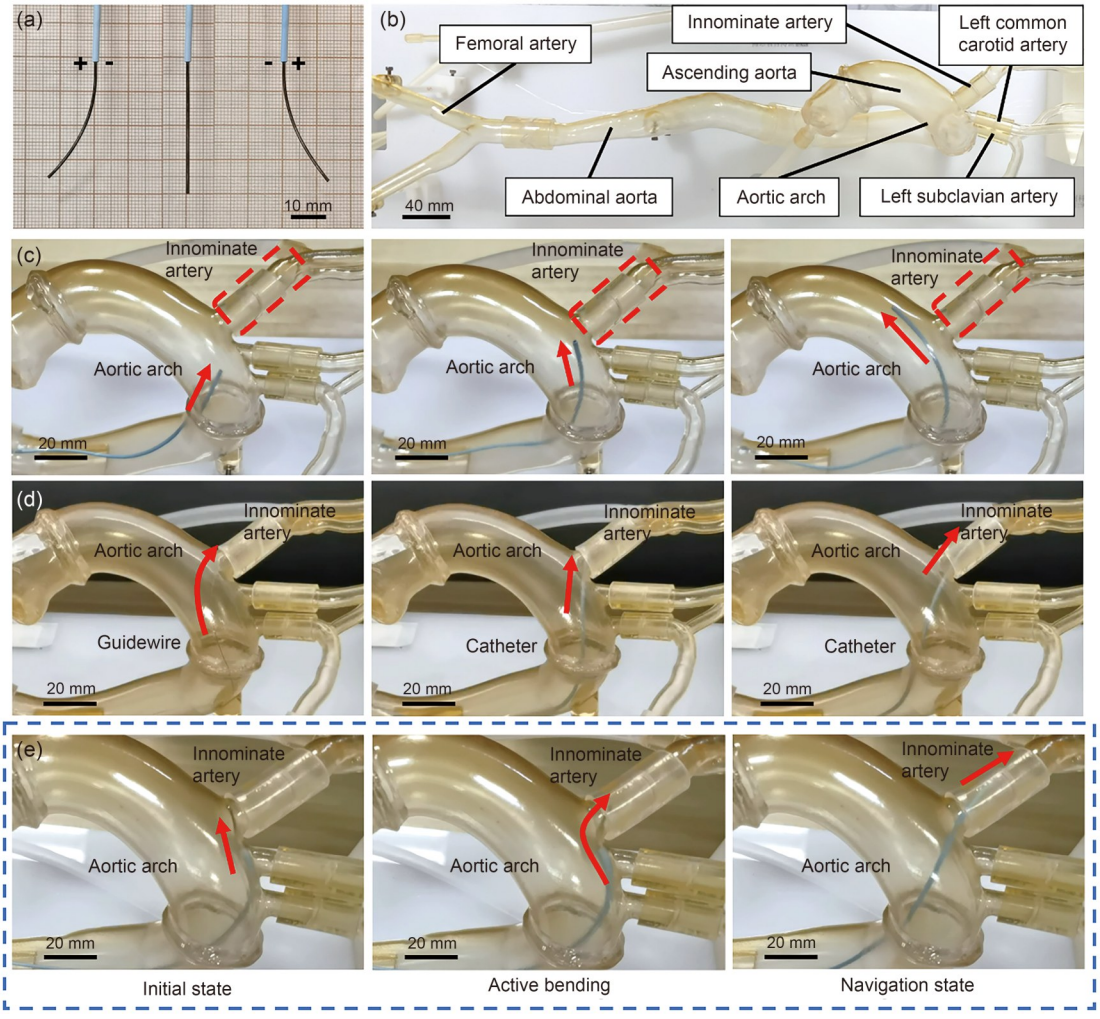

Fig. 4 Active navigation of the electrically driven steerable interventional catheters in a human vascular model. (a) Optical image of the bending deformation of the MTi actuator-based steerable interventional catheter under 7 V. (b) Overall display of the three-dimensional human vascular model. (c) Limitation of traditional interventional catheters in the selection of the branches of the aortic arch. (d) Entry of a guidewire-led traditional interventional catheter into the innominate artery. (e) The steerable interventional catheter can achieve active bending to select a vascular branch, enabling its entry into the innominate artery

actuators were used at the tip of the catheters for active navigation. A human blood vessel model prepared by 3D printing was employed in this in vitro experiment based on the conventional vascular disease treatment (Fig. 4b). The ratio of the size of the arterial blood vessels in this model to that of an adult male is 1:1. During the in vitro experiment, the bending angle and movement direction of the MTi actuators were controlled using a DC power supply to realize active navigation of the catheters in the human vascular model. Meanwhile, to compare the performance of these catheters

with the traditional ones, two in vitro groups were set using this human blood vessel model: one using conventional interventional catheters for navigation without guidewires (Fig. 4c), and the other set of catheters guided by a guidewire (Fig. 4d).

In the human blood vessel model, traditional interventional catheters required repeated pushing, pulling, and twisting with the assistance of a guidewire to reach the innominate artery (Fig. 4d; Movie S3 in the supplementary information). In contrast, the steerable interventional catheter can smoothly navigate to the innominate artery without the need for a guidewire. As it entered the innominate artery from the aortic arch, the angle of the vascular branch increased to about 90°. At this vascular branch, electrical voltage was applied to the steerable interventional catheters, causing the catheter's tip to actively bend and successfully enter the innominate artery (Fig. 4e; Movie S4 in the supplementary information). Furthermore, the steerable interventional catheters can navigate more smoothly to the left subclavian and left common carotid arteries compared to traditional catheters (Fig. S12 and Movies S5–S8 in the supplementary information). As shown in Table 2, the steerable interventional catheters navigated the innominate, left subclavian, and left common carotid arteries at 34.3%–48.3% less time than traditional catheters with guidewires. In contrast, conventional catheters without the MTi actuators cannot reach these areas without the aid of guidewires. Moreover, they were difficult to control as they passed through the vascular branches, even bending into the ascending aorta (Fig. 4c; Movie S9 in the supplementary information). Even with guidewires, the traditional catheters required more time to enter these arteries. Therefore, the results of the in vitro vascular model experiments demonstrate that steerable interventional catheters can smoothly enter the next vessel via bending deformation of the MTi actuators under applied voltage, indicating their excellent navigation function. This is expected to reduce surgical difficulty and improve surgical efficiency.

3.4 In vivo evaluation of the MTi actuator-based steerable interventional catheters in a porcine model

To verify the safety and accuracy of the steerable interventional catheters in selecting vascular branches in vivo, experiments were performed using a porcine model (Fig. 5a). As shown in Fig. 5b, the vascular distribution of the pig's innominate artery is relatively narrower and more branched compared to that in humans, making this a suitable site to test the active navigation ability of the steerable interventional catheters. During the surgical process, the imaging status of the steerable interventional catheters, the performance of vascular branch selection, the potential damage to the vascular wall, and the duration of the surgery were recorded. First, the arterial vascular distribution of the innominate artery was observed through subtraction angiography (Fig. 5c; Movie S10 in the supplementary information). The 8F arterial sheath was inserted through the left femoral artery, and then a steerable interventional catheter was inserted through the arterial sheath for detection. After reaching the innominate artery, a voltage was applied to make the catheters bend forward into the right subclavian artery (Fig. 5d; Movie S11 in the supplementary information). By continuously applying voltage, the steerable interventional catheters can be manipulated to withdraw from the innominate artery and enter the common carotid and right common carotid arteries (Fig. 5e; Movie S12 in the supplementary information). The same procedure can be used to manipulate the catheters to return to the common carotid artery and then select the left common carotid artery (Fig. 5f; Movie S13 in the supplementary information).

Besides the active navigation under electrical voltage stimulation, the steerable interventional catheters also achieved continuous delivery of contrast medium into the left ventricle. As shown in Fig. 6 and Movies S14 and S15 (supplementary information), the steerable interventional catheters could quickly and accurately navigate from the aortic arch to the left ventricle (Fig. 6a). Subsequently, the contrast medium was successfully delivered through the hollow structure of MTi actuators at the end of the catheters (Fig. 6b). These catheters can also be used to dispense agents, such as lipiodol, gelatin sponge, and microspheres for thrombus formation, and chemotherapy drugs such as cisplatin, epirubicin, pirarubicin, mitomycin, and 5-fluorouracil for treating solid tumors. The entire surgical process can significantly reduce damage caused to the blood vessels.

After surgery, the steerable interventional catheters and vascular sheath were removed from the pig's body, and then the local blood vessels were ligated. The Bama miniature pig was returned to the animal room.

Table 2 Comparison of efficiency for traditional and steerable interventional catheters

Location	Time (s)		Efficiency improvement
	Traditional interventional catheters with guidewires	Steerable interventional catheters	
Innominate artery	89	51	42.7%
Left subclavian artery	67	44	34.3%
Left common carotid artery	87	45	48.3%

Time is measured from the entry of the guidewire/catheter into the innominate artery until the completion of its advancement into the target artery

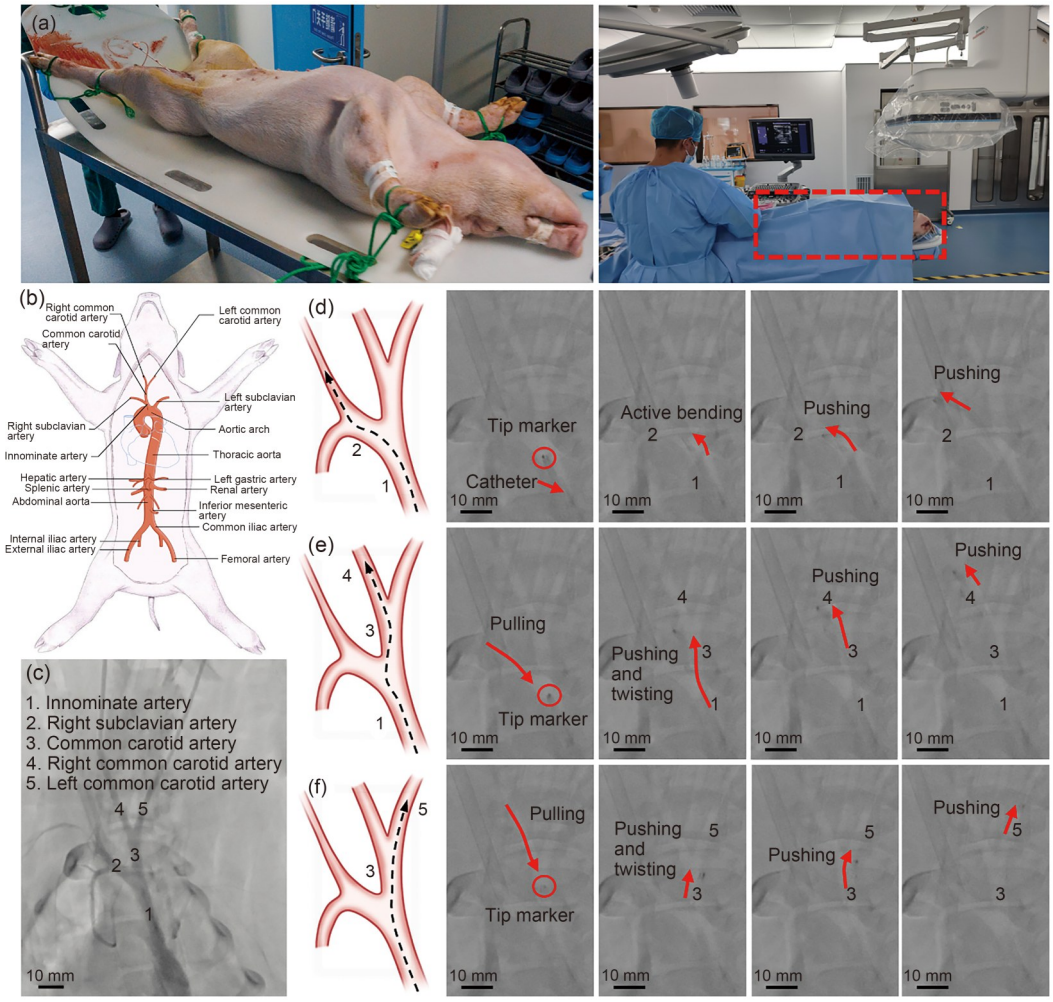

Fig. 5 In vivo animal experiments using steerable interventional catheters. (a) Images of the live pig used for the animal experiment. (b) Schematic of the porcine arteries. (c) Diagnostic subtraction angiography of the innominate artery. The steerable interventional catheters were manipulated to enter the right subclavian artery from the innominate artery (d), the right common carotid artery from the innominate artery (e), and the left common carotid artery from the common carotid artery (f)

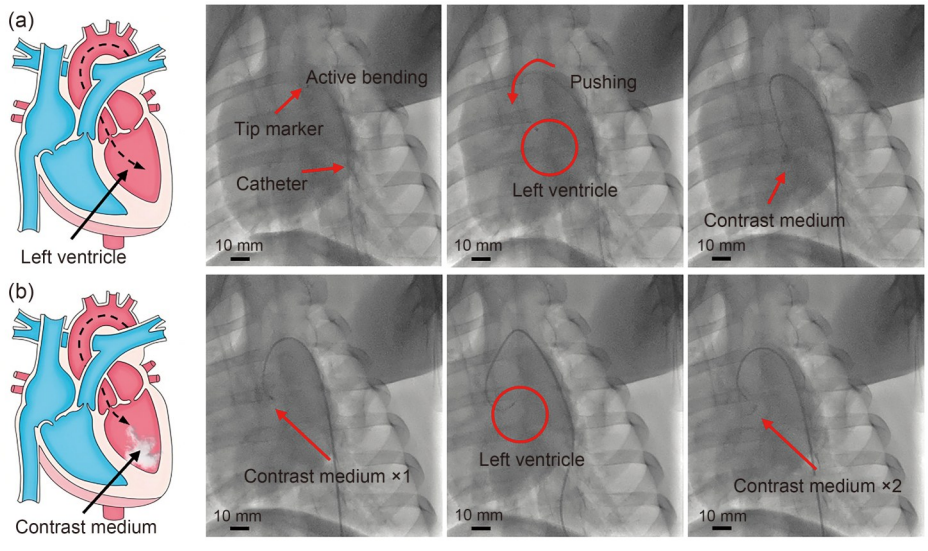

Fig. 6 In vivo animal experiments of active navigation and drug delivery of the catheters in the porcine left ventricle. The use of steerable interventional catheters to navigate into the left ventricle (a) and to continuously deliver the contrast medium (b)

4 Conclusions

In conclusion, steerable interventional catheters based on electrically driven MTi actuators were developed in this study. These catheters can actively bend within blood vessels to achieve successful navigation and drug delivery. MTi actuators, with outer diameters of 0.6 and 0.8 mm, were fabricated by the chemical plating technique. The improved electrochemical performance of these actuators facilitated large reversible bending deformation of these catheters under low-voltage (4–7 V DC) stimulation. Therefore, these actuators are promising candidates for the active navigation of interventional catheters in vivo. The active navigation capability of these MTi actuator-based steerable catheters was analyzed using a human vascular model, which included the main pathways for aneurysm embolization and interventional therapy (femoral artery–common iliac artery–abdominal aorta–aortic arch–innominate artery/left subclavian artery/left common carotid artery). The results showed that the steerable interventional catheters can quickly and accurately select the vessel branches to safely reach the desired location under the navigation of the MTi actuators, even in vessels with multiple branches. In contrast, traditional catheters required more twisting and manipulation to reach the desired direction and position, increasing the risk of blood vessel damage. Further experiments in a porcine model demonstrated that the steerable interventional catheters achieved active bending and selectively engaged vessel branches in porcine arteries. These catheters successfully entered the left and right common carotid arteries, the right subclavian artery, and the left ventricle, without the need for guidewires. Furthermore, the hollow structure of the MTi actuators facilitated the delivery of the contrast medium into the left ventricle. The steerable interventional catheters are designed to accommodate various blood vessel sizes, including renal, hepatic, coronary, and intracranial arteries, for thrombolysis therapy or thrombectomy treatment of thrombosis. Furthermore, these catheters can facilitate the arterial injection of chemotherapy drugs into solid tumors.

Supplementary Information The online version contains supplementary material available at https://doi.org/10.1631/bdm.2500183.

Acknowledgements The authors acknowledge funding from the National Natural Science Foundation of China (No. 52375293), the Research Fund of State Key Laboratory of Mechanics and Control for Aerospace Structures (Nanjing University of Aeronautics and astronautics, Nos. 1005-IZD2300225 and IZD2400217), the Nanjing Life and Health Technology Special Project (No. 202305031), the Clinical Competence Enhancement Project in Healthcare (No. JSPH-MB-2022-4), and the Medical Engineering Translational Fund of Jiangsu Province Hospital (No. NM202402).

Author contributions Conceptualization, QSH, SYL, and XFL; methodology, QSH, SYL, XFL, and WXG; investigation, QSH, SYL, XFL, ZHL, XS, and JJD; visualization, QSH, SYL, XFL, YH, LFC, TW, YZY, QYZ, XYL, and WMX; supervision, QSH, SYL, XFL, JFZ, YH, FJZ, CCZ, and YL; writing—original draft, QSH, SYL, and XFL; writing—review & editing, QSH, SYL, YH, DW, and YL; resources and validation, QSH, SYL, XFL, WXG, YFH, WQL, YZY, QYZ, YFW, YG, and YL.

Declarations

Conflict of interest The authors declare that they have no conflict of interest.

Ethical approval Animal procedures were conducted according to the ethical regulations reviewed and approved by the Institutional Animal Care and Use Committee (approval No. IACUC-2306014) at the First Affiliated Hospital with Nanjing Medical University.

Data availability The datasets used during the current study are available from the corresponding authors upon reasonable request.

References

1. Chai CL, Pyeong Jeon J, Tsai YH et al (2020) Endovascular intervention versus surgery in ruptured intracranial aneurysms in equipoise: a systematic review. Stroke 51(6):1703–1711. https://doi.org/10.1161/STROKEAHA.120.028798
2. Molyneux AJ, Kerr RSC, Birks J et al (2009) Risk of recurrent subarachnoid haemorrhage, death, or dependence and standardised mortality ratios after clipping or coiling of an intracranial aneurysm in the International Subarachnoid Aneurysm Trial (ISAT): long-term follow-up. Lancet Neurol 8(5):427–433. https://doi.org/10.1016/S1474-4422(09)70080-8
3. Fan JH, Ren SQ, Han B et al (2024) Magnetic fiber robots with multiscale functional structures at the distal end. Adv Funct Mater 34(12):2309424. https://doi.org/10.1002/adfm.202309424
4. Dreyfus R, Boehler Q, Lyttle S et al (2024) Dexterous helical magnetic robot for improved endovascular access. Sci Robot 9(87):eadh0298. https://doi.org/10.1126/scirobotics.adh0298
5. Wang L, Zheng DC, Harker P et al (2021) Evolutionary design of magnetic soft continuum robots. Proc Natl Acad Sci USA 118(21): e2021922118. https://doi.org/10.1073/pnas.2021922118
6. Li N, Fei P, Tous C et al (2024) Human-scale navigation of magnetic microrobots in hepatic arteries. Sci Robot 9(87):eadh8702. https://doi.org/10.1126/scirobotics.adh8702
7. Jung J, Penning RS, Zinn MR (2014) A modeling approach for robotic catheters: effects of nonlinear internal device friction. Adv Robot 28(8):557–572. https://doi.org/10.1080/01691864.2013.879371
8. Xu K, Simaan N (2010) Intrinsic wrench estimation and its performance index for multisegment continuum robots. IEEE Trans Robot 26(3):555–561. https://doi.org/10.1109/TRO.2010.2046924
9. Gerboni G, Henselmans PWJ, Arkenbout EA et al (2015) HelixFlex: bioinspired maneuverable instrument for skull base surgery. Bioinspiration Biomim 10(6):066013. https://doi.org/10.1088/1748-3190/10/6/066013
10. Gopesh T, Wen JH, Santiago-Dieppa D et al (2021) Soft robotic steerable microcatheter for the endovascular treatment of cerebral disorders. Sci Robot 6(57):eabf0601. https://doi.org/10.1126/scirobotics.abf0601
11. Ikuta K, Matsuda Y, Yajima D et al (2012) Pressure pulse drive: a

control method for the precise bending of hydraulic active catheters. IEEE/ASME Trans Mechatron 17(5):876–883. https://doi.org/10.1109/TMECH.2011.2138711
12. Ikuta K, Ichikawa H, Suzuki K et al (2006) Multi-degree of freedom hydraulic pressure driven safety active catheter. In: Proceedings IEEE International Conference on Robotics and Automation, p.4161–4166. https://doi.org/10.1109/ROBOT.2006.1642342
13. Rus D, Tolley MT (2015) Design, fabrication and control of soft robots. Nature 521(7553):467–475. https://doi.org/10.1038/nature14543
14. Phan PT, Hoang TT, Thai MT et al (2022) Twisting and braiding fluid-driven soft artificial muscle fibers for robotic applications. Soft Robot 9(4):820–836. https://doi.org/10.1089/soro.2021.0040
15. Christianson C, Goldberg NN, Deheyn DD et al (2018) Translucent soft robots driven by frameless fluid electrode dielectric elastomer actuators. Sci Robot 3(17):eaat1893. https://doi.org/10.1126/scirobotics.aat1893
16. Abdelaziz MEMK, Zhao JS, Gil Rosa B et al (2024) Fiberbots: robotic fibers for high-precision minimally invasive surgery. Sci Adv 10(3):eadj1984. https://doi.org/10.1126/sciadv.adj1984
17. Ayvali E, Liang CP, Ho M et al (2012) Towards a discretely actuated steerable cannula for diagnostic and therapeutic procedures. Int J Rob Res 31(5):588–603. https://doi.org/10.1177/0278364912442429
18. Haga Y, Esashi M (2000) Assembly of bending, torsional and extending active catheter using electroplating. IEEJ Trans Sens Micromach 120(11):515–520. https://doi.org/10.1541/ieejsmas.120.515
19. Sheng J, Wang XF, Dickfeld TML et al (2018) Towards the development of a steerable and MRI-compatible cardiac catheter for atrial fibrillation treatment. IEEE Robot Autom Lett 3(4): 4038–4045. https://doi.org/10.1109/LRA.2018.2861011
20. Selvaraj M, Takahata K (2020) Electrothermally driven hydrogel-on-flex-circuit actuator for smart steerable catheters. Micromachines 11(1):68. https://doi.org/10.3390/mi11010068
21. Mineta T, Mitsui T, Watanabe Y et al (2001) Batch fabricated flat meandering shape memory alloy actuator for active catheter. Sens Actuat A Phys 88(2):112–120. https://doi.org/10.1016/S0924-4247(00)00510-0
22. Yun CH, Yeo LY, Friend JR et al (2012) Multi-degree-of-freedom ultrasonic micromotor for guidewire and catheter navigation: the NeuroGlide actuator. Appl Phys Lett 100(16):164101. https://doi.org/10.1063/1.3702579
23. Santa AD, Mazzoldi A, de Rossi D (1996) Steerable microcatheters actuated by embedded conducting polymer structures. J Intell Mater Syst Struct 7(3):292–300. https://doi.org/10.1177/1045389x9600700309
24. Fang BK, Ju MS, Lin CK (2007) A new approach to develop ionic polymer–metal composites (IPMC) actuator: fabrication and control for active catheter systems. Sens Actuat A Phys 137(2): 321–329. https://doi.org/10.1016/j.sna.2007.03.024
25. Jo C, Pugal D, Oh IK et al (2013) Recent advances in ionic polymer–metal composite actuators and their modeling and applications. Prog Polym Sci 38(7):1037–1066. https://doi.org/10.1016/j.progpolymsci.2013.04.003
26. Ma SQ, Zhang YP, Liang YH et al (2020) High-performance ionic-polymer–metal composite: toward large-deformation fast-response artificial muscles. Adv Funct Mater 30(7):1908508. https://doi.org/10.1002/adfm.201908508
27. Shahinpoor M, Kim KJ (2000) The effect of surface-electrode resistance on the performance of ionic polymer-metal composite (IPMC) artificial muscles. Smart Mater Struct 9(4):543–551. https://doi.org/10.1088/0964-1726/9/4/318
28. Liu CB, Xu H, Liang YH et al (2023) High water content electrically driven artificial muscles with large and stable deformation for soft robots. Chem Eng J 472:144700. https://doi.org/10.1016/j.cej.2023.144700
29. Olsen ZJ, Kim KJ (2022) Characterizing the transduction behavior of ionic polymer-metal composite actuators and sensors via dimensional analysis. Smart Mater Struct 31(2):025014. https://doi.org/10.1088/1361-665X/ac411e
30. Wang H, Yang L, Yang YN et al (2023) Highly flexible, large-deformation ionic polymer metal composites for artificial muscles: fabrication, properties, applications, and prospects. Chem Eng J 469:143976. https://doi.org/10.1016/j.cej.2023.143976
31. Shahinpoor M, Kim KJ (2001) Ionic polymer-metal composites: I. fundamentals. Smart Mater Struct 10(4):819. https://doi.org/10.1088/0964-1726/10/4/327
32. Lu C, Chen W, Zhang XH (2025) Highly efficient ionic actuators enabled by sliding ring molecule actuation. Nat Commun 16(1): 2480. https://doi.org/10.1038/s41467-025-57893-5
33. Wu G, Hu Y, Liu Y et al (2015) Graphitic carbon nitride nanosheet electrode-based high-performance ionic actuator. Nat Commun 6:7258. https://doi.org/10.1038/ncomms8258
34. He QS, Yin GX, Vokoun D et al (2022) Review on improvement, modeling, and application of ionic polymer metal composite artificial muscle. J Bionic Eng 19(2):279–298. https://doi.org/10.1007/s42235-022-00153-9
35. He QS, Liu ZG, Yin GX et al (2020) The highly stable air-operating ionic polymer metal composite actuator with consecutive channels and its potential application in soft gripper. Smart Mater Struct 29(4):045013. https://doi.org/10.1088/1361-665X/ab73e3
36. He QS, Yang X, Wang ZY et al (2017) Advanced electro-active dry adhesive actuated by an artificial muscle constructed from an ionic polymer metal composite reinforced with nitrogen-doped carbon nanocages. J Bionic Eng 14(3):567–578. https://doi.org/10.1016/S1672-6529(16)60422-5
37. Guo SX, Fukuda T, Kosuge K et al (1996) A study on active catheter system (3rd Report, Modeling and experimental results of "in vitro" of active guide wire catheter using ICPF actuator). Trans Japan Soc Mech Eng Ser C 62(596):1384–1391 (in Japanese). https://doi.org/10.1299/kikaic.62.1384
38. Fang BK, Lin CK, Ju MS (2010) Development of sensing/actuating ionic polymer–metal composite (IPMC) for active guidewire system. Sens Actuat A Phys 158(1):1–9. https://doi.org/10.1016/j.sna.2009.12.001
39. He QS, Huo K, Xu XR et al (2020) The square rod-shaped ionic polymer-metal composite and its application in interventional surgical guide device. int J Smart Nano Mater 11(2):159–172. https://doi.org/10.1080/19475411.2020.1783020
40. Kim SJ, Pugal D, Wong J et al (2014) A bio-inspired multi degree of freedom actuator based on a novel cylindrical ionic polymer–metal composite material. Robot Auton Syst 62(1):53–60. https://doi.org/10.1016/j.robot.2012.07.015
41. Ruiz S, Mead B, Palmre V et al (2015) A cylindrical ionic polymer-metal composite-based robotic catheter platform: modeling, design and control. Smart Mater Struct 24(1):015007. https://doi.org/10.1088/0964-1726/24/1/015007
42. Tsugawa MA, Palmre V, Carrico JD et al (2015) Slender tube-shaped and square rod-shaped IPMC actuators with integrated

sensing for soft mechatronics. Meccanica 50(11):2781–2795. https://doi.org/10.1007/s11012-015-0218-9
43. Horiuchi T, Asaka K (2019) 245 mm length IPMC catheter with an ellipse-like cross-section. Smart Mater Struct 28(9):095028. https://doi.org/10.1088/1361-665X/ab1cf0
44. Horiuchi T, Sugino T, Asaka K (2017) Elliptical-like cross-section ionic polymer-metal composite actuator for catheter surgery. Sens Actuat A Phys 267:235–241. https://doi.org/10.1016/j.sna.2017.10.002
45. Lu C, Zhao L, Hu YM et al (2018) A molecular-regulation strategy towards low-voltage driven, multi degree of freedom IPMC catheters. Chem Commun 54(63):8733–8736. https://doi.org/10.1039/C8CC04967J
46. Muller DW, Shamir KJ, Ellis SG et al (1992) Peripheral vascular complications after conventional and complex percutaneous coronary interventional procedures. Am J Cardiol 69(1):63–68. https://doi.org/10.1016/0002-9149(92)90677-q
47. Pierot L, Biondi A (2016) Endovascular techniques for the management of wide-neck intracranial bifurcation aneurysms: a critical review of the literature. J Neuroradiol 43(3):167–175. https://doi.org/10.1016/j.neurad.2016.02.001
48. Lin N, Brouillard AM, Krishna C et al (2015) Use of coils in conjunction with the pipeline embolization device for treatment of intracranial aneurysms. Neurosurgery 76(2):142–149. https://doi.org/10.1227/NEU.0000000000000579
49. Lanzer P (2013) Catheter-Based Cardiovascular Interventions (1st Ed.). Springer Berlin, Germany. https://doi.org/10.1007/978-3-642-27676-7
50. Nhat NLQ, Nguyen Truong T (2015) Development of the bending actuator with Nafion-Pt IPMC tube. Adv Mater Res 1119: 251–257. https://doi.org/10.4028/www.scientific.net/amr.1119.251